Statistical Analysis of Real Aperture Radar Field Backscattered From Sea Surfaces Under Moderate Winds by Monte Carlo Simulations

Nicolas Pinel, *Member, IEEE*, Bertrand Chapron, Christophe Bourlier, *Associate Member, IEEE*, Nicole de Beaucoudrey, René Garello, *Fellow, IEEE*, and Antoine Ghaleb

Abstract—The statistical properties of the electromagnetic field backscattered from sea surfaces are studied by using asymptotic numerical methods. Sea surfaces are modeled by using the Elfouhaily *et al.* spectrum model. The influence of the radar spatial resolution on the field statistics is studied for various wind conditions and radar configurations, by considering equal range and azimuth resolutions. It is observed that the backscattered field phase can be assimilated to a uniform distribution and that the amplitude resembles a Rayleigh distribution. Moreover, reducing the radar spatial resolution d induces a stronger variability of the backscattered field amplitude and a departure from the Rayleigh distribution. This departure is enhanced particularly when the radar look approaches the cross-wind direction and also when increasing the wind speed. Also, a fitting of the amplitude distribution with various theoretical statistical laws (gamma, Weibull, K, and so on) highlights the general good fitting of the K distribution, which is in agreement with previous work led from measurements.

Index Terms—Monte Carlo process, real aperture radar (RAR), sea surface electromagnetic (EM) scattering, statistical study.

I. INTRODUCTION

THE MODENA[1] project aims at modeling and simulating the maritime environment remotely sensed by a radar [1], [2]. In this context, in order to build a realistic simulator of the sea clutter observed by a real aperture radar (RAR), RAR backscattered field statistics are needed.

[1]The MODENA (for modeling of the remote sensing of the maritime environment) project received a distinction of quality from the Brittany Center of Excellence called "Pôle Mer." It was funded by a grant from the Direction Générale des Entreprises (DGE), the Brittany Region, the Département du Finistère, and the Brest Métropole Océane.

Modeling electromagnetic (EM) field statistics in coherent imaging is an active research area, and different statistical distributions have been proposed [3]–[8]. The empirical models describe the statistical behavior of the field emitted by a radar (including its amplitude and its phase) and backscattered from the sea surface as derived from measurements. It was observed that the amplitude departs from a Rayleigh distribution as the radar spatial resolution gets better and that the phase resembles a uniform distribution [9]. Numerous papers have been published about empirical modeling of the statistics of high-resolution sea clutter data [10]–[15]. Except from the very basic Rayleigh distribution, classical used distributions are mainly log-normal, Weibull, gamma, and K distributions [11], [12], [14], [15]. The K distribution is probably the most often used distribution and seems to be a good candidate, at least for low-grazing incidence angles [16]. An important drawback of analyzing data is the uncertainties in the experimental conditions as well as their variations during the measurements, which makes the interpretation difficult. Also, the EM scattering from sea surfaces is a complex phenomenon, in general, because it involves many different physical behaviors: single or multiple scattering, wave asymmetry, wave breaking, sea foam, etc. All of these different phenomena are complex to analyze simply because they often contribute simultaneously. Then, numerical simulation models can be of great help to better understand and analyze data statistics. This is one of the aims of this paper. An important advantage of this approach is the exact knowledge of the simulation conditions.

Numerical models can now efficiently be implemented to simulate sea-like surfaces generated from appropriate surface spectra (such as Elfouhaily *et al.* [17]), for a specified spatial resolution of the radar. Statistical distributions can then be derived from a sufficient number of computations. As such, the statistical distributions can be refined (both their types and the values of their parameters), and most importantly, the dependence of the radar spatial resolution on the field statistics can be studied. In this context, with the help of the increase of computing resources, numerical simulation models for deriving the backscattered field statistics begin to appear in the literature [18]–[21]. Nevertheless, for sea-like surfaces, modeling sea surface radar backscattering by numerical simulations remains a challenging task. That is why numerical simulations use simplifications, like studying 2-D (2-D) problems only [19], [20], applying asymptotic models [18], [21], or working at the

lower frequencies (typically, L-band rather than X-band) of the radar band [20], [21].

Here, we deal with realistic 3-D problems at X-band by applying asymptotic models and by studying the influence of several parameters (the radar spatial resolution, the incidence angle, the wind speed and direction) on the backscattered field statistics. Focus is made on the field amplitude (modulus), by comparison with the classical Rayleigh distribution.

This paper is organized as follows. Section II presents the hydrodynamic model and the surface generation process. Section III studies the constraints on the minimum size of surface to be generated in order to correctly describe the EM problem by studying the incoherent normalized radar cross section (NRCS) and the backscatter amplitude correlation. Section IV studies the backscattered field statistical properties by focusing on the amplitude. The influence of various parameters (the radar resolution, the incidence angle, and the wind speed and direction) is analyzed, as well as the fitting with several distributions: particularly the Weibull, K, and gamma distributions.

II. HYDRODYNAMIC MODEL AND SURFACE GENERATION

In order to correctly predict the mechanisms of scattering from sea-like surfaces, beforehand, an appropriate hydrodynamic modeling of concerned rough surfaces is necessary. For a 3-D problem, the generation of a so-called 2-D sea surface is necessary, from the knowledge of an appropriate surface height spectrum S_h. Here, we consider the widely used Elfouhaily et al. spectrum model [17], which is known to correctly describe the surface height spectrum for fully developed seas at moderate wind speeds u_{10}. The sea surface height distribution is assumed to be Gaussian, and the surfaces are generated by convolution of a white Gaussian noise; then, surface nonlinearities (like the one given by Creamer or choppy-wave transforms) are not introduced here.

At X band, the sea surface conductivity is high; then, the Leontovich impedance boundary condition can be used (the relative permittivity is taken here for $f = 10$ GHz as $\epsilon_r = 53.2 + 37.8i$). This allows us to sample the surface with the same sampling step as that for a perfectly conducting surface; otherwise, this would be too prohibitive. To solve the EM problem which considers a very conducting medium, surfaces must be generated with a spatial sampling step $\Delta x = \Delta y$ on the order of $\lambda_0/8$ (ideally, the sampling step is rather $\lambda_0/10$). Here, we will take $\Delta x = \Delta y = \lambda_0/8$, which corresponds to $\Delta x = \Delta y = 0.375$ cm at a radar frequency $f = 10$ GHz (corresponding to a wavelength in vacuum $\lambda_0 = 3$ cm). Moreover, under the Elfouhaily et al. spectrum model, the surface wavenumber k_p (called peak wavenumber) at which the height spectrum S_h is maximum is given by [17]

$$k_p \simeq \Omega^2 g/u_{10}^2 \qquad (1)$$

with g being the acceleration due to gravity, usually taken as 9.81 m/s^2, and Ω being the inverse wave age, usually taken as 0.84 for fully developed seas. Then, for $u_{10} = 5$ m/s and $u_{10} = 7$ m/s, the peak wavenumbers $k_p \simeq 0.277$ rad/m and $k_p \simeq 0.141$ rad/m, respectively, which correspond to surface peak
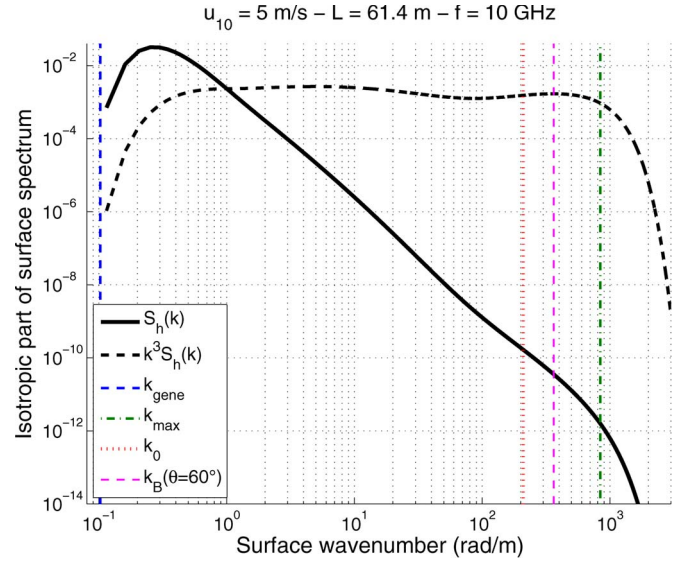

Fig. 1. Isotropic part of the Elfouhaily et al. surface height $S_h(k)$ and curvature $k^3 S_h(k)$ spectra versus the surface wavenumber, for a wind speed $u_{10} = 5$ m/s. The EM wavenumber $k_0 = 2\pi/\lambda_0$ is plotted as a red dotted line for $f = 10$ GHz, the wavenumber $k_{\max} = \pi/\Delta_x = \pi/\Delta_y$ corresponding to the generated surface sampling step $\Delta_x = \Delta_y = \lambda_0/8$ is plotted as a green dash-dot line, and the surface wavenumber $k_{\text{gene}} = 2\pi/L$ associated to the generated surface length L is plotted as a blue dashed line for $N_{\text{ech}} = 16\,384^2$. The Bragg wavenumber $k_B = 2k_0 \sin\theta$ is also plotted for an incidence angle from zenith $\theta = 60°$.

wavelengths $L_p \simeq 22.7$ m and $L_p \simeq 44.5$ m, respectively. As a consequence, in order to be able to simulate the field backscattered by an infinite 2-D sea surface (i.e., for which the surface gravity waves are correctly represented), the generated square sea surface must have a length $L_x = L_y \equiv L$ much larger than the so-called "surface peak wavelength" L_p. This corresponds to having a square sea surface with a number of samples N_{ech} checking $N_{\text{ech}} \gg (6,052)^2$ and $N_{\text{ech}} \gg (11,861)^2$ for $u_{10} = 5$ m/s and $u_{10} = 7$ m/s, respectively.

Usually, it is said that, to correctly take the gravity waves into account in the surface spectrum, the minimum surface wavenumber $k_{\min}$, corresponding to the minimum length of the surface to be generated, should check the condition $k_{\min} \simeq 0.3k_p$ [22]. Then, for a frequency $f = 10$ GHz and by taking a spatial sampling step $\Delta x = \Delta y = \lambda_0/8$, the corresponding minimum number of samples $N_{\text{ech,min}}$ should be $N_{\text{ech,min}} \gtrsim (20,173)^2$ and $N_{\text{ech,min}} \gtrsim (39,537)^2$ for $u_{10} = 5$ m/s and $u_{10} = 7$ m/s, respectively. This is a very hard constraint to follow, particularly for a surface generation with MATLAB. We will see in Section III that, for incidence angles away from $0°$, fortunately a slightly looser constraint may be applied in practice. This point is illustrated in Fig. 1 from the isotropic part of the Elfouhaily et al. surface height spectrum for a wind speed $u_{10} = 5$ m/s and for a number of samples of generated surface $N_{\text{ech}} = 16\,384^2$. In this figure, it can be seen that, for a radar frequency $f = 10$ GHz, the associated wavenumber k_0 corresponds to a high-frequency component of the surface spectrum or, in other words, belongs to the capillary wave regime. This also holds (and it is even more pronounced) for the maximum wavenumber $k_{\max}$, which is the wavenumber associated to the generated surface sampling step, i.e., $k_{\max} = 4k_0$ here. Finally, for studied generated surfaces with $N_{\text{ech}} = 16\,384^2$ samples,
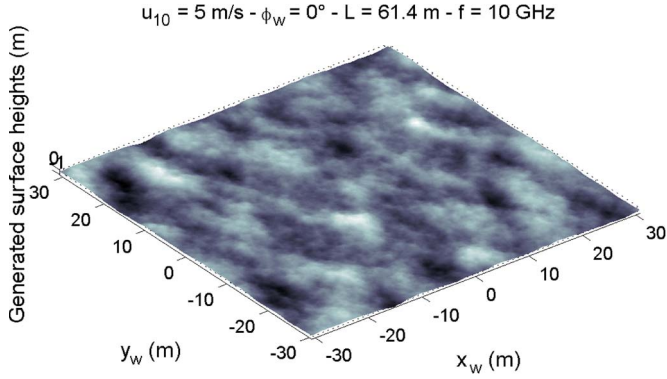
Fig. 2. Illustration of a generated sea surface for a wind speed $u_{10} = 5$ m/s and a wind direction with respect to the x_w-axis $\phi_w = 0$. The surface is made of $N_{ech} = 16\,384^2$ samples with sampling step $\Delta_x = \Delta_y = \lambda_0/8$ at $f = 10$ GHz so that the surface has a length $L = 61.4$ m.

corresponding to a surface length $L = 61.4$ m, the associated wavenumber $k_{gene} = 2\pi/L$ is not much less than k_p: It does not check the condition $k_{gene} < 0.3k_p$. This means that, for these generated surfaces, which is one of the largest surfaces that our office PC can generate and process, the gravity waves of the sea surface are significantly truncated.

Correspondingly, Fig. 2 shows an illustration of a generated sea surface for a wind speed $u_{10} = 5$ m/s and a wind direction with respect to the x_w-axis $\phi_w = 0$. The surface is made of $N_{ech} = 16\,384^2$ samples with sampling step $\Delta_x = \Delta_y = \lambda_0/8$, with $f = 10$ GHz, so that the surface has a length $L = 61.4$ m.

Thus, a quantitative analysis of the influence of this truncation on the EM wave backscattering must be studied in the following.

III. SIMULATED BACKSCATTERING AND MINIMUM GENERATED SURFACE LENGTH

The aforementioned qualitative analysis clearly illustrates the difficulty of computing the 3-D EM wave backscattering from sea surfaces at centimeter-scale wavelengths with numerical methods. To our knowledge, this number of unknowns is prohibitive for rigorous numerical methods and very likely even if acceleration processes are used. Thus, to resolve numerically this typical problem here, asymptotic models are used. More precisely, the so-called "local" models are applied, such as the Kirchhoff-tangent plane approximation (KA) with its high-frequency regime (KAHF), the first-order small slope approximation (SSA1), the weighted curvature approximation (WCA), etc. [23]. Here, we will focus on two local models, namely, the SSA1 and the WCA, which are usually called "unified" models: Indeed, contrary to the KAHF model which is valid for high frequencies and thus applicable to sea surface backscattering for rather low incidence angles (i.e., near zenith direction), the "unified" models were built to be applicable in the whole range of (nongrazing) incidence angles. The scattering amplitude, which is proportional to the backscattered field, is given under the KAHF by the relation [24], [25]

$$\mathbb{S}(\boldsymbol{k}, \boldsymbol{k_0}) = \frac{\mathbb{K}(\boldsymbol{k}, \boldsymbol{k_0})}{Q_z} \int_{\boldsymbol{r}} e^{-jQ_z\eta(\boldsymbol{r})} e^{-j\boldsymbol{Q_H}\cdot\boldsymbol{r}} d\boldsymbol{r} \quad (2)$$

where $\mathbb{K}(\boldsymbol{k}, \boldsymbol{k_0})$ is the so-called KAHF kernel, which is a polarization term, and $\boldsymbol{Q_H}$ and Q_z are the horizontal and vertical components of the vector $\boldsymbol{Q} = \boldsymbol{k} - \boldsymbol{k_0}$, respectively, with $\boldsymbol{k_0}$ and $\boldsymbol{k}$ being the incidence and observation wave vectors. The scattering amplitude under the SSA1 is given by [24], [25]

$$\mathbb{S}(\boldsymbol{k}, \boldsymbol{k_0}) = \frac{\mathbb{B}(\boldsymbol{k}, \boldsymbol{k_0})}{Q_z} \int_{\boldsymbol{r}} e^{-jQ_z\eta(\boldsymbol{r})} e^{-j\boldsymbol{Q_H}\cdot\boldsymbol{r}} d\boldsymbol{r} \quad (3)$$

where $\mathbb{B}(\boldsymbol{k}, \boldsymbol{k_0})$ is the first-order small perturbation model (SPM1) kernel. Finally, the scattering amplitude under the WCA is given by [24], [25]

$$\mathbb{S}(\boldsymbol{k}, \boldsymbol{k_0}) = \frac{1}{Q_z} \int_{\boldsymbol{r}} e^{-jQ_z\eta(\boldsymbol{r})} e^{-j\boldsymbol{Q_H}\cdot\boldsymbol{r}}$$
$$\times \left[\mathbb{B}(\boldsymbol{k}, \boldsymbol{k_0}) - \mathbb{T}(\boldsymbol{k}, \boldsymbol{k_0}; -Q_z\boldsymbol{\gamma}) \right] d\boldsymbol{r} \quad (4)$$

where $\mathbb{T}(\boldsymbol{k}, \boldsymbol{k_0}; \boldsymbol{\xi}) = \mathbb{B}((\boldsymbol{k} + \boldsymbol{k_0} + \boldsymbol{\xi})/2, (\boldsymbol{k} + \boldsymbol{k_0} - \boldsymbol{\xi})/2) - \mathbb{K}((\boldsymbol{k} + \boldsymbol{k_0} + \boldsymbol{\xi})/2, (\boldsymbol{k} + \boldsymbol{k_0} - \boldsymbol{\xi})/2)$ and $\boldsymbol{\gamma} = \boldsymbol{\nabla}\eta = [(\eta/x) (\eta/y)]$, with $\mathbb{B}$ being the SPM1 kernel and $\mathbb{K}$ being the KAHF kernel. The polarization dependence of the three models is given by the KAHF and SPM1 kernels. Then, in what follows, when studying the normalized amplitude which is equivalent to studying the normalized scattering amplitude (the normalization is made by dividing the amplitude by the root mean square of the average cross section), for both the KAHF and the SSA1 models, the constant term (kernel divided by Q_z) before the numerical integration in (2) and (3) is suppressed. Therefore, the result is independent of the polarization. Moreover, as the numerical integration is identical for both models, they give the same normalized results. On the contrary, for the WCA model, the polarization term (kernel) is inside the numerical integration: It is then not suppressed by the normalization.

Nevertheless, even if such rather simple models are used for numerical computations on office computers with MATLAB, the aforementioned constraint remains hard to satisfy. However, for a monostatic configuration at nonnormal incidence angles θ_0 ($\theta_0 \in \{30°; 45°; 60°\}$ here), the gravity waves do not necessarily need to be represented very precisely. Still, the acceptable limit remains to be determined. That is why it is suggested here to study the influence of the surface length L on the accuracy of the incoherent NRCS computed by asymptotic numerical models, by comparison with both analytical computations and an experimental model [26]. For the sea surfaces being generated by using an inverse Fourier transform of the spectrum, the number of samples is chosen as power-2 to be able to use an inverse fast Fourier transform.

A. NRCS and Minimum Generated Surface Length

Fig. 3 represents the incoherent monostatic NRCS versus the incidence angle of a sea surface with wind speed $u_{10} = 5$ m/s for downwind direction $\Delta\phi = \phi_0 - \phi_w = 0$ (with ϕ_0 being the radar direction, at a frequency $f = 10$ GHz and in HH polarization. A comparison of the SSA1 from both numerical ("SSA1n") and analytical ("SSA1a") computations is presented, together with the KA with high-frequency regime
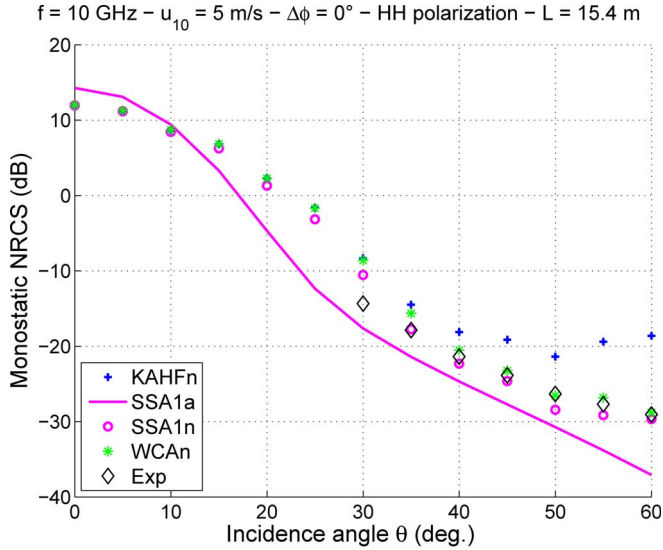
Fig. 3. Incoherent monostatic NRCS versus the incidence angle of a sea surface with wind speed $u_{10} = 5$ m/s and direction $\Delta\phi = \phi_0 - \phi_w = 0$ for a frequency $f = 10$ GHz in HH polarization: comparison of the KAHF, the WCA, and the SSA1 from both numerical and analytical computations. For the numerical computations, $N_{surf} = 200$ surfaces of length $L = 15.4$ m were generated. Results from an experimental model [26] are also plotted.

approximation (KAHF) and the WCA from numerical computations. For the numerical computations, $N_{surf} = 200$ surfaces of length $L = 15.4$ m were generated. The results are also compared with the experimental model of Masuko *et al.* [26]. For this surface length, the number of surface samples is $N_{ech} = 2^{12} \times 2^{12} = 4096^2$. It can be observed that, for moderate incidence angles $35° \lesssim \theta \lesssim 50°$, the agreement of the numerical methods with the analytical SSA1, which includes all of the components of the spectrum, is rather correct (but with a nonnegligible overestimation). By contrast, for small or high incidence angles $0° \leq \theta \lesssim 30°$ or $55° \lesssim \theta \leq 60°$, the agreement of the two numerical methods with the analytical method is poor. This is also the case (and even worse) for smaller surface lengths. Similar remarks hold for the comparison with the experimental model which should, in general, be superior to the simulations, as the latter do not take several physical phenomena into account (multiple scattering, whitecaps, etc.). This condition is clearly not fulfilled for $0 \leq \theta < 35°$. Fig. 4 represents the same simulation parameters as in Fig. 3, except for the generated surface length $L = 61.4$ m. Moreover, the number of realizations is $N_{surf} = 13$. This corresponds to a number of surface samples (for each generated surface) $N_{ech} = 2^{14} \times 2^{14} = 16\,384^2$, with 2^{14} being nearly the maximum power-2 number our office PC (Dual Intel Xeon X5650 2×6 cores at 2.67-GHz frequency, with 32 Go DDR2-type RAM) can handle by using MATLAB. Comparatively to Fig. 3, there is also a good agreement (and even better) for moderate incidence angles, as well as a much better agreement for small incidence angles, particularly at $\theta = 30°$ where a good agreement is found. Thus, for $\theta = \{30°, 45°, 60°\}$, which are the angular configurations used to establish the field statistics in the following, a rather good agreement with the analytical SSA1 results, and the experimental model can be observed for this surface length. This should validate the use of this surface
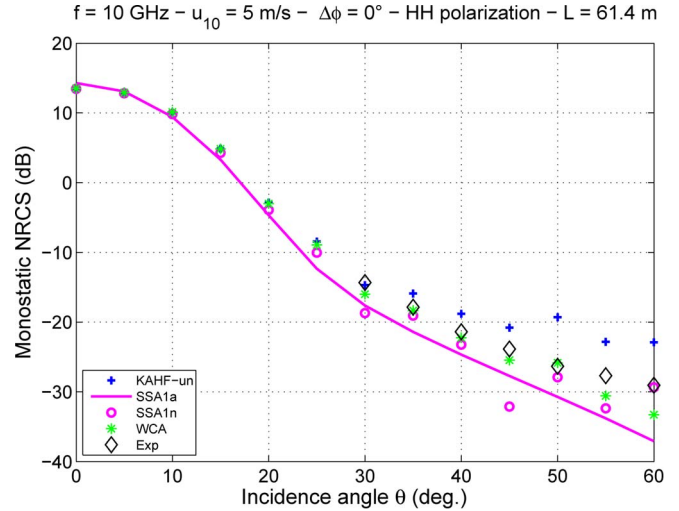

Fig. 4. Same simulation parameters as in Fig. 3, except for the generated surface length $L = 61.4$ m (with $N_{surf} = 13$).

length at this typical frequency, at least for the lower wind speed $u_{10} = 5$ m/s. Similar remarks and conclusion can be made for the other configurations by varying the wind direction and/or the wind speed.

Similarly as in [19], these results will be confirmed in the following by analyzing the backscatter spatial autocorrelation. Indeed, a physical condition on the minimum generated surface length is that the backscattered field autocorrelation tends to 0 near the edges of the surface: If this condition is not checked, then, by generating several independent surfaces by a Monte Carlo process, we do not correctly simulate the backscattered field from a theoretically infinite surface. This is then a necessary condition for having the right to split up the theoretically infinite surface into its summation of independent limited size surfaces.

B. Backscattered Field Autocorrelation and Minimum Generated Surface Length

Fig. 5 plots an example of the simulated backscattered field amplitude RAR image from the generation of a single sea surface, under the WCAn model in VV polarization. The simulation parameters are the following: incidence angle $\theta = 45°$, azimuth angle with respect to the wind direction $\Delta\phi = 90°$ (i.e., the wind blows along the y-axis), and wind speed $u_{10} = 7$ m/s. The radar operates at $f = 10$ GHz and has a spatial resolution $d_x = d_y \equiv d = 0.5$ m. Generated sensed surface is made of $N_{ech} = 16\,384^2$ samples with sampling step $\Delta_x = \Delta_y = \lambda_0/8$. Here, radar resolution is achieved in a way similar to what is described in [21, pp. 4188–4189]. Nevertheless, it has been tested that the use of a window function (such as Gaussian beams) for the incident wave is not necessary for this situation. Then, for computing the backscatter from every pixel (or square resolution cell) of the surface, the considered incident beam is a plane wave (without Gaussian window); the calculation is then made by assuming a single-frequency continuous wave (like in [21]) within each square resolution cell.

This figure illustrates the spatial variability of the backscattered field amplitude for a given radar spatial resolution. Here, it
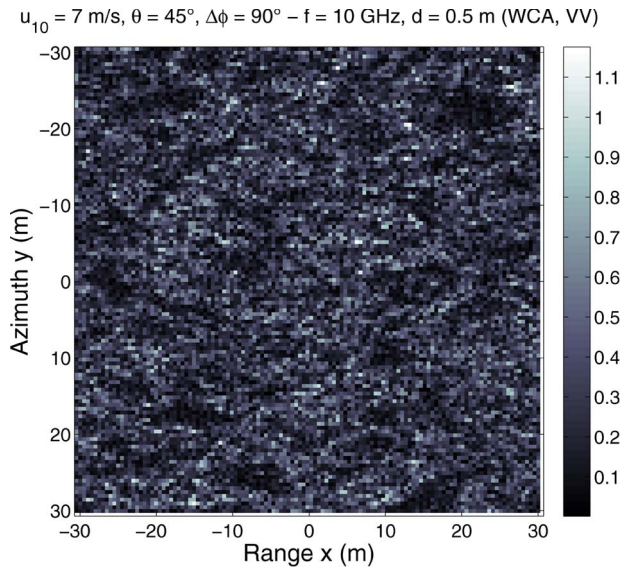
Fig. 5. Illustration of the RAR image simulated with the WCAn in VV polarization from a single generated sea surface for a wind speed $u_{10} = 7$ m/s. The surface is made of $N_{\text{ech}} = 16\,384^2$ samples with sampling step $\Delta_x = \Delta_y = \lambda_0/8$, with $f = 10$ GHz, so that the surface has a length $L = 61.4$ m. The radar has a spatial resolution $d_x = d_y \equiv d = 0.5$ m, a configuration of incidence angle $\theta = 45°$, and an azimuth angle with respect to the wind direction $\Delta\phi = 90°$ (i.e., the wind blows along the y-axis).
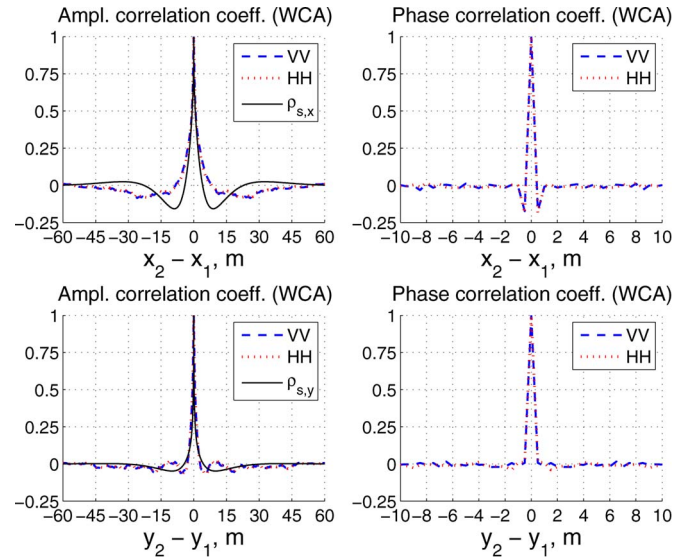

Fig. 6. Average correlation coefficients of the backscattered field amplitude (left) or phase (right) with respect to the range x (up) or the azimuth y (down) after averaging over the corresponding orthogonal direction for the same parameters as in Fig. 5 and by averaging over 63 surfaces. A comparison is also made with the surface slope autocorrelation coefficient ρ_s of generated surfaces.

can be observed that the spatial correlation between the echoes is stronger in varying the range direction x than in the azimuth direction y. It is interesting to note that the range direction x corresponds to the cross-wind direction, as the radar azimuthal direction with respect to the wind direction $\Delta\phi = 90°$ ($\Delta\phi$ is defined with respect to the x direction). This result is not surprising, as the surface slope variations are smaller in the cross-wind direction than the downwind direction. Then, the sea surface heights and slopes vary much more significantly in the y direction than in the x direction, which implies a much more significant spatial variation of the backscattered field amplitude. This visual qualitative observation will be confirmed in the next figure analyzing quantitatively the amplitude autocorrelation. The HH polarization (not presented here) shows very similar features, with a little bit more spiky shape.

Sea echoes can be described by coherent and incoherent covariance functions [19], [27]. Here, for the purpose of studying the minimum generated surface length, we are interested in autocovariance functions. More precisely, for having a fair description of the backscattered field statistics, the autocorrelation of the backscatter from a given surface must tend to 0 near the edges of the surface.

Fig. 6 shows the amplitude (left) and phase (right) average correlation coefficients with respect to the radar range direction x (up) and the radar azimuth direction y (down; after averaging over the other direction) derived for the same parameters as in Fig. 5 (after averaging over 63 surfaces) for both VV and HH polarizations of the WCA model. More precisely, for the amplitude, like in [19, Fig. 6] for a 2-D problem, we study the noncoherent backscatter and compare the results with the surface slope autocorrelation coefficients ρ_s of generated surfaces with respect to corresponding x and y directions ($\rho_{s,x}$ and $\rho_{s,y}$, respectively). It can be seen that, for both x and y

directions, the average phase correlation coefficients tend to 0 very fast. For the y direction, it reaches 0 as soon as the first departure from $y_1 = y_2$, i.e., 0.5-m distance here. For the x direction, it reaches approximately -0.2 at 0.5-m distance and reaches 0 afterward. Moreover, the VV and HH polarizations do not highlight significant differences.

The average amplitude correlation coefficients in x and y directions highlight features similar to the phase correlation coefficients, but they both take negative values and tend to 0 much more slowly, especially for the x direction. Indeed, in this direction, they tend to 0 only when $x_1 - x_2 \simeq 55$ m, near the edges of the surface. This means that, for this typical configuration, the minimum surface length to be generated to correctly describe the EM backscattering is on the order of 55 m, which is reached here. Other simulations for varying parameters (not plotted here) show that decreasing the incidence angle θ or increasing the wind speed u_{10} or moving the azimuth direction $\Delta\phi$ closer to the upwind or downwind look ($\Delta\phi = 0°$ or $180°$) leads to a slower decrease of the correlation coefficients. This implies that the minimum surface length to be generated increases for these cases. Comparing the VV and HH polarizations of the WCA, only slight differences appear around the minimum of the function. Finally, comparing them to the surface slope autocorrelation coefficient ρ_s, a rather good general agreement can be observed for this typical configuration where local models (such as the WCA) can be applied. This is not surprising because we know that the so-called two-scale model [28]–[31], which is directly related to the slope of the facet, can be applied here. Nevertheless, a necessary condition for this agreement is that the length of the generated surface must be greater than the minimum surface length such that the average amplitude correlation coefficients tend to 0 at the edges of the surface.

Thus, after checking the conditions for correctly describing the backscattered field from sea surfaces, the specific study of its statistics can be led. Hereafter, we focus on the amplitude statistics. The phase always resembles a uniform distribution. The real and imaginary parts depart from Gaussian distributions when the amplitude departs from a Rayleigh distribution. This behavior is studied more thoroughly in the following section by varying different physical parameters such as the radar spatial resolution d, the incidence angle θ, the azimuth angle with respect to the wind direction $\Delta\phi$, and the wind speed u_{10}.

IV. BEHAVIOR OF BACKSCATTERED FIELD STATISTICS WITH RESPECT TO RADAR CONFIGURATION

A. Context

In order to have enough backscattered field data N_{data} to build the statistical distributions, a large number N_{surf} of trials (or surface generations) must be performed. For a fixed number of generated surfaces N_{surf}, this number of data points N_{data} depends on the radar spatial resolution d (see [32, Table I]). Ideally, N_{data} should be taken on the order of 10 000 [7]. The surfaces are generated from the Elfouhaily *et al.* spectrum model [17], as described in Sections II and III.

The following scenarios were investigated: For an X-band radar with frequency $f = 10$ GHz, we consider two moderate wind speeds $u_{10} = 5$ m/s and $u_{10} = 7$ m/s; three azimuth angles with respect to the wind direction $\Delta\phi = 0°$, $\Delta\phi = 45°$, and $\Delta\phi = 90°$; and three incidence angles $\theta_0 = 30°$, $\theta_0 = 45°$, and $\theta_0 = 60°$. For each scenario, we study the influence of the radar resolution (or, in other words, the patch dimensions) on the statistical distributions (both their types and the values of their parameters) by taking various resolutions such as $d_x = d_y \equiv d = \{0.5; 1; 2; 4; 6; 8; 10\}$ m. More importantly, another goal is to investigate when the amplitude distribution departs from a Rayleigh distribution and, in that case, how the distribution can be fitted.

From the generation of a significant number N_{surf} of sea surfaces, for a given configuration (with a given radar spatial resolution d), a statistical analysis of the backscattered field can be led in both amplitude (modulus) and phase, as well as in both real and imaginary parts. For all simulations that follow, we recall the following common parameters: The frequency $f = 10$ GHz, and the surfaces are sampled at $\Delta_x = \Delta_y = \lambda_0/8$, with a number of samples $N_{\text{ech}} = 16\,384^2$, corresponding to a surface length $L = 61.4$ m. The number of generated surfaces $N_{\text{surf}} = 63$. Knowing that the total number of statistical data N_{data} is related to the number of generated square surfaces N_{surf} and the ratio of the surface length L over the radar resolution d through the equation $N_{\text{data}} = N_{\text{surf}}E(L/d)^2$ (with E being the integer part operator), for $d = \{0.5; 1; 2; 4; 6; 8; 10\}$ m, $N_{\text{data}} = \{937\,692; 234\,423; 56\,700; 14\,175; 6\,300; 3\,087; 2\,268\}$, respectively. First, before studying the influence of the configurations on the backscattered field amplitude statistics, let us have a look at the statistics of the amplitude and the phase, as well as of the real and imaginary parts.

Similarly to [9] and [19], the backscattered field is normalized before plotting. For the amplitude, the normalization is done by dividing the backscattered field data by the square
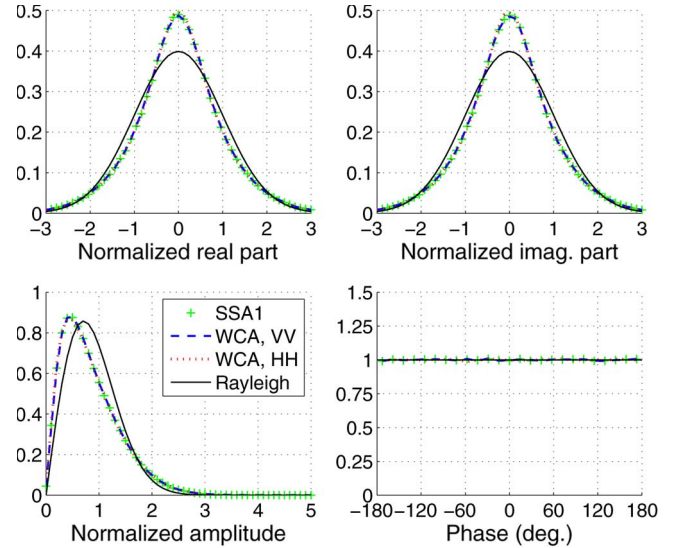

Fig. 7. Backscattered normalized field real part, imaginary part, amplitude, and phase statistics for the same configuration as in Fig. 5. Both VV and HH polarizations of the WCA are plotted, as well as the SSA1. For the real and imaginary parts, a comparison is made with a Gaussian distribution, and for the amplitude, a comparison is made with a Rayleigh distribution. For the phase, the computed distribution is normalized by 1 for better clarity.

root of the average cross section [9], [19]. Moreover, for the real and imaginary parts, in order to compare with a Gaussian distribution with zero mean and unitary standard deviation, the data are centered (i.e., mean subtracted) and then divided by their standard deviation. Finally, for the phase, the computed distribution is normalized by 1 for better clarity of the figure. Thus, by doing so, it is found that the KAHF (in either VV or HH polarization) and the SSA1 (in either VV or HH polarization) give the same results. This is not surprising, as these two models are related to each other (for a given configuration) by a constant polarization term. This constant term is suppressed after the normalization, which explains why we get the same observed results [see (2) and (3)]. As a consequence, in what follows, it is not necessary to plot each of the four cases: Giving the mean μ and standard deviation σ of the four cases and plotting only one case are enough. This case will be SSA1 (in VV polarization).

Fig. 7 plots the backscattered normalized field real part, imaginary part, amplitude, and phase statistics for the same configuration as in Fig. 5 for both VV and HH polarizations of the WCA and for the SSA1. First, for the phase statistics, it can be seen that the three models follow a uniform distribution. The real and imaginary parts show very similar behaviors between the three models. Also, they significantly depart from a Gaussian distribution: They all show a peaked behavior, which is the most pronounced for WCA in HH polarization and the less pronounced for WCA in VV polarization. Similar observations can be made for the amplitude statistics by comparison with the Rayleigh distribution, which can be seen as the consequence of the real and imaginary part behaviors. Indeed, if real and imaginary parts are independent and follow a Gaussian distribution with equal variance, then the amplitude follows a Rayleigh distribution. For information, the mean values μ of the KAHF, the SSA1, and the WCA nonnormalized amplitude

TABLE I

MEAN VALUE μ OF THE NONNORMALIZED AMPLITUDE STATISTICAL DATA AND MEAN VALUE μ_n (TO BE COMPARED TO $\sqrt{\pi/4} \simeq 0.886$ FOR THE RAYLEIGH DISTRIBUTION) AND STANDARD DEVIATION σ_n (TO BE COMPARED TO $\sqrt{1 - \pi/4} \simeq 0.463$ FOR THE RAYLEIGH DISTRIBUTION) OF THE NORMALIZED AMPLITUDE STATISTICAL DATA FOR BOTH, KAHF, SSA1, AND WCA MODELS IN BOTH VV (FIRST LINE) AND HH (SECOND LINE) POLARIZATIONS

| Fig. #	KAHF $(\mu; \mu_n, \sigma_n)$	SSA1 $(\mu; \mu_n, \sigma_n)$	WCA $(\mu; \mu_n, \sigma_n)$
Fig. 7, $u_{10} = 7$ m/s, $d = 0.5$ m, $\Delta\phi = 90°$, $\theta = 45°$	0.207; 0.842, 0.540	0.284; 0.842, 0.540	0.282; 0.842, 0.539
	0.207; 0.842, 0.540	0.111; 0.842, 0.540	0.114; 0.839, 0.544
Fig. 8, $u_{10} = 7$ m/s, $d = 2$ m, $\Delta\phi = 90°$, $\theta = 45°$	0.129; 0.872, 0.489	0.176; 0.872, 0.489	0.174; 0.874, 0.486
	0.129; 0.872, 0.489	0.069; 0.872, 0.489	0.072; 0.869, 0.496
Fig. 9, $u_{10} = 5$ m/s, $d = 0.5$ m, $\Delta\phi = 90°$, $\theta = 45°$	0.215; 0.854, 0.521	0.294; 0.854, 0.521	0.292; 0.854, 0.520
	0.215; 0.854, 0.521	0.115; 0.854, 0.521	0.117; 0.853, 0.522
Figs. 10-12, $u_{10} = 5$ m/s, $d = 0.5$ m, $\Delta\phi = 0°$, $\theta = 45°$	0.254; 0.867, 0.498	0.348; 0.867, 0.498	0.345; 0.868, 0.497
	0.254; 0.867, 0.498	0.136; 0.867, 0.498	0.140; 0.864, 0.503
Figs. 13-15, $u_{10} = 5$ m/s, $d = 0.5$ m, $\Delta\phi = 0°$, $\theta = 60°$	0.369; 0.872, 0.490	0.525; 0.872, 0.490	0.523; 0.872, 0.489
	0.369; 0.872, 0.490	0.104; 0.872, 0.490	0.106; 0.871, 0.491
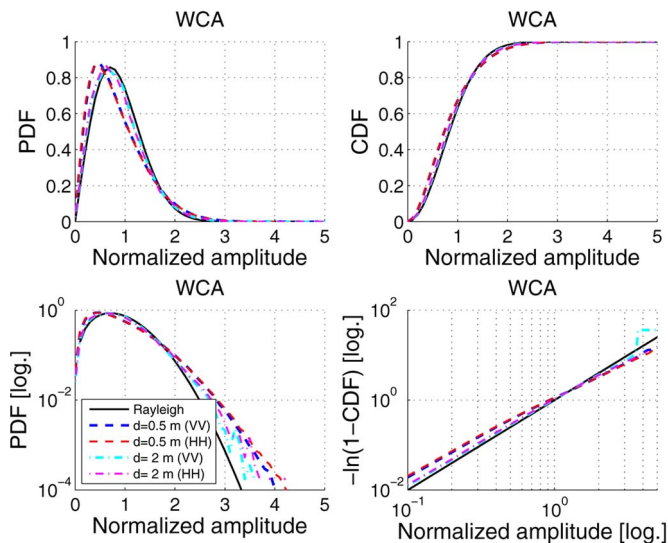
Fig. 8. Backscattered normalized field amplitude statistics for the same configuration as in Fig. 5 but for two radar spatial resolutions ($d = \{0.5, 2\}$ m). Both the VV and HH polarizations of the WCA are plotted. A comparison is made with a Rayleigh distribution. Linear (up) and logarithmic (down) scale figures are used.

distributions are reported in Table I for both VV (first line) and HH (second line) polarizations, as well as the mean value μ_n and standard deviation σ_n of these normalized amplitude distributions. Note that μ_n must be compared to $\sqrt{\pi/4} \simeq 0.886$ and σ_n to $\sqrt{1 - \pi/4} \simeq 0.463$ for the Rayleigh distribution.

In what follows, the study focuses on the amplitude statistics in order to investigate the influence of various physical parameters on the shape of the statistics, particularly its departure from the Rayleigh distribution, together with its fitting with other classical distributions.

B. Behavior of Backscattered Field Amplitude Statistics With Respect to Configuration

First, let us have a look at the influence of the configuration on the amplitude statistics. Fig. 8 plots the same parameters as in Fig. 5 but for two radar spatial resolutions ($d = \{0.5, 2\}$ m).

Both the VV and HH polarizations of the WCA are plotted. Also, the probability density function (pdf) is plotted on the two left figures, whereas the cumulative density function (CDF) is plotted in the upper right panel using the linear scale and in the lower right panel using the Weibull paper. Different spatial resolutions were tested: $d = \{0.5, 1, 2, 4, 6, 8, 10\}$ m, but not all were plotted for the clarity of the figure. It can be seen that decreasing the spatial resolution d from 2 m to 0.5 m induces a departure from the classical Rayleigh distribution. This departure is characterized by a shift of the maximum of the pdf to lower amplitude values and an increase of the maximum, as well as a heavier tail of the pdf. Like in Fig. 7 for $d = 0.5$ m, slight differences appear here for $d = 2$ m between VV and HH polarizations. For instance, a slight shift of the maximum and a slightly heavier tail of the pdf occur for HH polarization. As expected, it can be seen from Table I that increasing the spatial resolution d leads to a lower variability of the normalized amplitude (see σ_n values for all models and polarizations): It gets closer to that of the Rayleigh distribution.

Fig. 9 plots the same parameters as in Fig. 8 but by varying the wind speed u_{10} instead of the resolution d: $u_{10} = \{5, 7\}$ m/s, with $d = 0.5$ m. Hereafter, only the pdf is plotted for better clarity of the figures. It can be seen that increasing the wind speed induces a more peaked pdf around its maximum and a heavier tail of the pdf. Moreover, comparing the results for the two polarizations, increasing u_{10} induces a larger difference between the two polarizations. Similarly, it can be seen in Table I that increasing u_{10} increases the variability σ_n of the amplitude for all cases and deviates from that of the Rayleigh distribution. Similar observations can be made for increasing the incidence angle θ_0 or moving the radar look relative direction $\Delta\phi$ away from the (up- or down-) wind direction [32].

C. Comparison of Backscattered Field Amplitude Statistics With Classical Distributions

Second, a study of the distributions that best fit the data is led. For doing so, one interesting means is the Pearson graph, for determining the type of Pierson distribution that must be
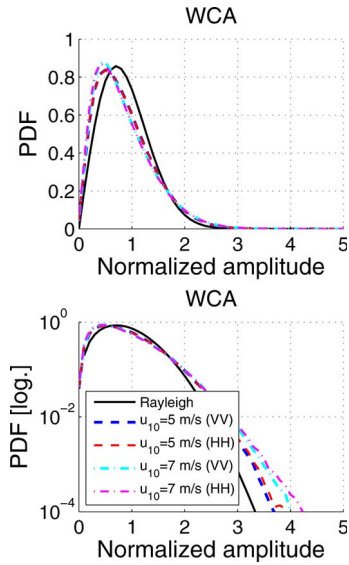
Fig. 9. Same parameters as in Fig. 8 but variations of the wind speed u_{10} instead of the resolution d: $u_{10} = \{5, 7\}$ m/s, with $d = 0.5$ m.
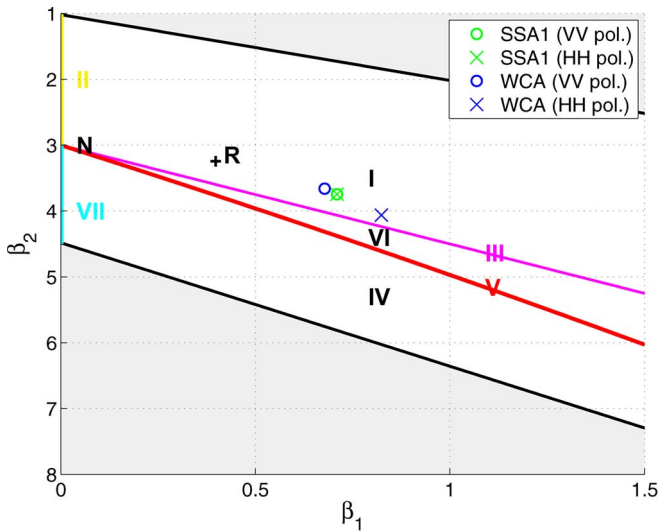

Fig. 10. Pearson graph for the same configuration as in Fig. 5, except for the wind speed $u_{10} = 5$ m/s and direction $\Delta\phi = 0°$. Both the VV and HH polarizations of the SSA1 and the WCA are plotted.

used, depending on the skewness and kurtosis of the normalized amplitude. This ranges from the Pearson distribution of type I to type VII, as described in [10], [33], and [34]. Several classical distributions are tested, such as the Weibull, K, and gamma distributions. In the Pearson graph, β_1 and β_2 are the square of the skewness and the kurtosis of the normalized amplitude, respectively: $\beta_1 = m_3{}^2/m_2{}^3$, and $\beta_2 = m_4{}^2/m_2{}^4$, with m_γ being the γth order centered moment. Note that the normal and Rayleigh distributions correspond to $\{\beta_1 = 0, \beta_2 = 3\}$ and $\{\beta_1 \simeq 0.398, \beta_2 \simeq 3.245\}$, respectively, as indicated by N and R in the Pearson graphs to be plotted hereafter.

Fig. 10 plots the Pearson graph of the SSA1 and the WCA models for both VV and HH polarizations, for the same configuration as in Fig. 5, except for the wind speed $u_{10} = 5$ m/s and direction $\Delta\phi = 0°$. The KAHF results are not reported here, as they give the same results as the SSA1 ones, owing
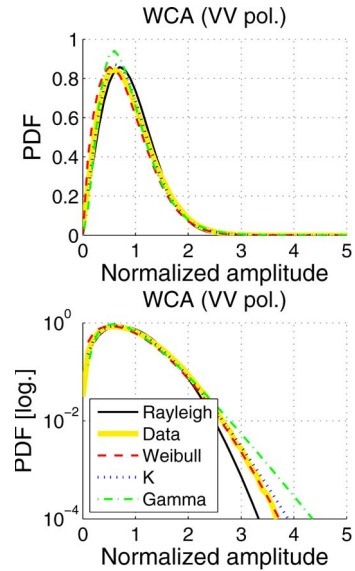

Fig. 11. Backscattered normalized field amplitude statistics for the same configuration as in Fig. 10 but for the VV polarization of the WCA model only. A comparison is made with classical distributions: first, the Rayleigh distribution but also the Weibull, K, and gamma distributions.

to the normalization. For the SSA1 model, it can be observed that the VV and HH polarizations give the same results, owing to the same reason. They belong to the Pearson-I type area and are rather close to the Pearson-III type limit. By contrast, for the WCA model, the VV and HH polarizations differ from each other and from the SSA1 model. The VV polarization of the WCA is rather close to the SSA1. It is a bit farther from the Pearson-III type limit. The HH polarization of the WCA is very close to the Pearson-III type limit. Note that the Pearson-III type distribution corresponds to the gamma distribution. Then, it is expected that the agreement with the gamma distribution is significantly better for the HH polarization than that for the VV polarization of the WCA model.

Then, Fig. 11 plots the corresponding backscattered normalized field amplitude statistics for the VV polarization of the WCA model, with the comparison with classical distributions: first, the Rayleigh distribution but also the Weibull, K, and gamma distributions. Let us highlight here that, although the log-normal distribution is often used, it generally gives significantly poorer agreement than the aforementioned other distributions. That is why it is not plotted here. First, it can be seen that the amplitude statistics slightly departs from the Rayleigh distribution. This difference is significant in linear scale around the maximum of the distribution and in logarithmic scale in the tail of the distribution. This difference also appears in the CDF (cumulative distribution function), particularly for the smaller values of the distribution (not shown here). The comparison of the amplitude statistics with the Weibull, K, and gamma distributions highlights a general good agreement with these three distributions, particularly the Weibull and K ones. Indeed, it can be seen that they both predict very well the general shape of the pdf, as well as its tail. The same general observations can be made for the CDF, even if observable differences occur when plotted on Weibull paper (not shown here). The Weibull distribution gives a slightly better agreement for the
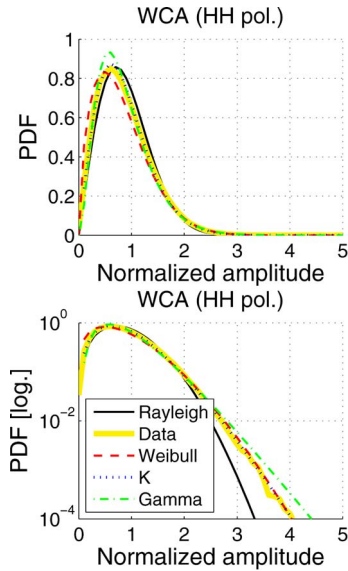
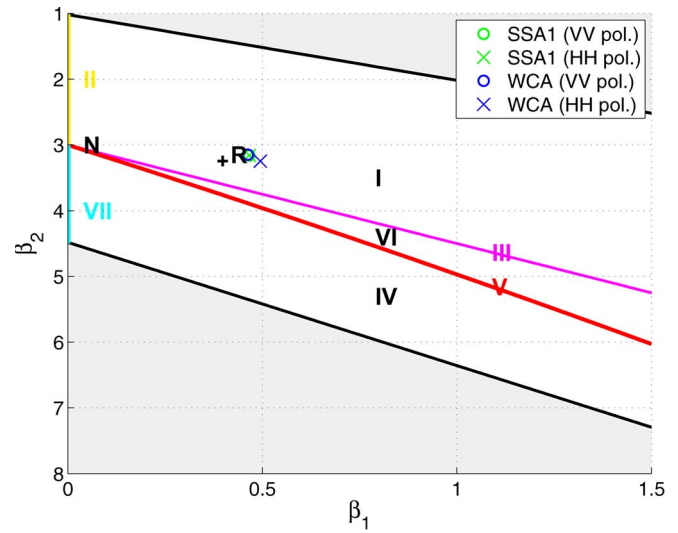Fig. 12. Same parameters as in Fig. 11 but for the HH polarization of the WCA model.

Fig. 13. Pearson graph for the same configuration as in Fig. 5, except for the wind speed $u_{10} = 5$ m/s and direction $\Delta\phi = 0°$, and for the incidence angle $\theta_0 = 60°$. Both the VV and HH polarizations of the SSA1 and the WCA are plotted. Then, this figure differs from Fig. 10 by $\theta_0 = 60°$ instead of $\theta_0 = 45°$.

pdf, whereas the K distribution gives the best agreement for the CDF (not shown here). A Kolmogorov-Smirnov goodness-of-fit test gives probabilities of 0.53, 0.70, 0.71, and 0.38 for Rayleigh, Weibull, K, and gamma distributions, respectively; then, they are all valid hypotheses within the significance level of $\alpha = 5\%$. Moreover, comparing Fig. 11, for which $\Delta\phi = 0°$, with the first set of curves of Fig. 9, for which $\Delta\phi = 90°$, it can be seen that, for this typical configuration, moving the wind direction $\Delta\phi$ closer to the cross-wind direction induces a departure from the Rayleigh distribution. This is in agreement with the statistical parameters in Table I: From $\Delta\phi = 0°$ to $\Delta\phi = 90°$, the variability σ_n of the normalized amplitude increases and gets away from that of the Rayleigh distribution.

Fig. 12 plots the same parameters as in Fig. 11 but for the HH polarization of the WCA model. The same observations can be made when comparing the amplitude statistics with the Rayleigh distribution. Similar observations can be made for the comparison with the Weibull, K, and gamma distributions. The main differences with the VV polarization are the following: The K distribution gives the best agreement for all cases. The Weibull distribution gives a slightly not as good agreement as the K distribution and as for VV polarization, contrary to the gamma distribution which gives a better match, as predicted by the Pearson graph. It is highlighted that the better agreement to the gamma distribution for HH than for VV polarization confirms the predictions of the Pearson graph, particularly for the tail of the pdf. The results from the SSA1 (not plotted here), as predicted by the Pearson graph, show intermediate results between those of the VV and HH polarizations of the WCA. A Kolmogorov-Smirnov goodness-of-fit test gives probabilities of 0.04, 0.96, 1.00, and 0.96 for Rayleigh, Weibull, K, and gamma distributions, respectively; then, they are all valid hypotheses within the significance level of $\alpha = 5\%$, except for the Rayleigh distribution.

Finally, let us study the influence of the incidence angle θ_0: It is changed from $\theta_0 = 45°$ in Fig. 10 to $\theta_0 = 60°$ in Fig. 13. Comparatively to Fig. 10, it can be seen that changing θ_0 from
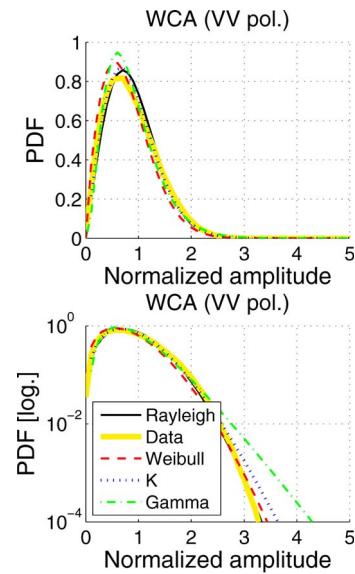

Fig. 14. Backscattered normalized field amplitude statistics for the same configuration as in Fig. 13 but for the VV polarization of the WCA model only. A comparison is made with classical distributions: first, the Rayleigh distribution but also the Weibull, K, and gamma distributions.

$45°$ to $60°$ leads to much less significant variations between the four cases and to a significant decrease of β_2 for all models and polarizations, as well as a decrease of β_1, whose amplitude slightly depends on the case. Then, all four cases belong to the type I area, this time, and are much closer to the Rayleigh distribution. Also, only slight differences between the four cases appear: Only the HH polarization of the WCA significantly differs from the other three cases. Thus, it is expected that the two polarizations of the WCA have only slightly different statistical behaviors.

Figs. 14 and 15 plot the corresponding backscattered normalized field amplitude statistics for the VV and HH polarizations of the WCA model, respectively, with a comparison with the Rayleigh distribution, as well as the Weibull, K, and gamma
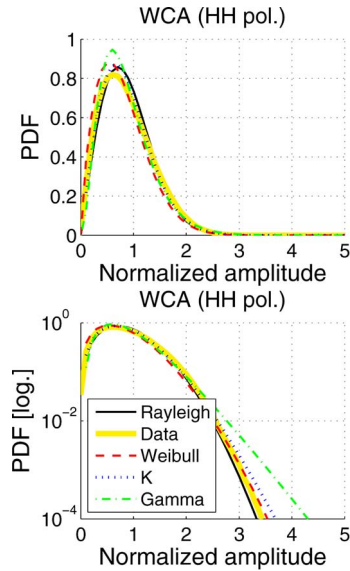
Fig. 15. Same parameters as in Fig. 13 but for the HH polarization of the WCA model.

distributions. It can be seen that the amplitude statistics slightly differs from the Rayleigh distribution for both polarizations. Significant differences between VV and HH polarizations appear only in the tail of the pdf with a heavier tail for the HH polarization, which is in agreement with the Pearson graph in Fig. 13. The comparison with the Weibull, K, and gamma distributions highlights a rather good agreement for mainly the K and Weibull distributions. The gamma distribution does not predict the pdf shape very well and fails to match the pdf tail. The Weibull distribution gives the best agreement, particularly for the HH polarization.

Comparatively to Figs. 11 and 12, where $\theta_0 = 45°$, the agreement with the gamma distribution is less good, which is again in agreement with the Pearson graphs, because of the departure from Person-III type limit. Moreover, the agreement with the Rayleigh distribution is better, particularly in the pdf tail. It is also in agreement with the Pearson graphs, as this configuration is closer to the Rayleigh case. Then, increasing the incidence angle θ_0 leads to a better agreement with the classical Rayleigh distribution here.

V. CONCLUSION

An analysis of the sea surface backscattered field statistics has been conducted for the case of the Elfouhaily *et al.* surface spectrum model [17] for fully developed seas, considering moderate wind speeds and moderate incidence angles. It was established that, in all studied cases, the phase can be assimilated to a uniform distribution. The field amplitude resembles a Rayleigh distribution for large enough radar resolutions d; correspondingly, the real and imaginary parts resemble Gaussian distributions.

It was established that the average correlation coefficient of the backscatter amplitude is strongly related to the surface slope autocorrelation function, as previously observed for 2-D problems [19]. Decreasing the radar resolution implies a greater variability of the field amplitude and a departure

from a Rayleigh distribution. This may be attributed to the spatial correlation between echoes. Similarly, increasing the wind speed from $u_{10} = 5$ m/s to $u_{10} = 7$ m/s implies a larger surface slope correlation length; thus, a greater variability of the field amplitude and a departure from a Rayleigh distribution are observed. Then, this may also be attributed to the spatial correlation between echoes.

For the field normalized amplitude statistics, the KAHF and SSA1 models show identical behaviors for both VV and HH polarizations. By contrast, for the WCA model, which depends not only on the surface heights but also on the surface slopes, the VV and HH polarizations may show significantly different features. Comparisons with different probability distribution models were conducted, particularly with the Weibull, K, and gamma distributions. Although the gamma distribution is not often used for analyzing statistical data, it gives, in general, a good agreement with the amplitude statistics, better than the log-normal distribution, for instance. Also, the Pearson graph is of good help to evaluate the gamma distribution fitting (which corresponds to the Pearson type III distribution): The fitting is better as the distribution skewness and kurtosis values approach the type III limit; a similar remark applies to the Rayleigh distribution fitting. The Weibull distribution and especially the K distribution also show good agreements, which is consistent with fitting procedures conducted in previous work with statistical measurement data [10]–[15].

REFERENCES

[1] R. Garello, "The MODENA project: Modeling and simulation of the maritime environment remotely sensed by radar," in *Proc. Oceans*, Quebec City, QC, Canada, Sep. 2008, pp. 1–5.

[2] A. Ghaleb, S. Even, R. Garello, B. Chapron, N. Pinel, N. de Beaucoudrey, F. Comblet, M. Parenthoen, and E. Pottier, "Modeling and simulation of sea surface radar observations," in *Proc. OCEANS MTS/IEEE SEATTLE*, Quebec City, QC, Canada, Sep. 2010, pp. 1–5.

[3] M. V. Berry, "The statistical properties of echoes diffracted from rough surfaces," *Philosoph. Trans. R. Soc. London A*, vol. 273, no. 1237, pp. 611–654, Feb. 1973.

[4] S. McDaniel, "Geometrical optics prediction of surface scattering statistics," *IEEE Trans. Geosci. Remote Sens.*, vol. 42, no. 2, pp. 361–366, Feb. 2004.

[5] I. Fuks and M. Charnotskii, "Statistics of specular points at a randomly rough surface," *J. Opt. Soc. Amer. A*, vol. 23, no. 1, pp. 73–80, Jan. 2006.

[6] S. Watson, E. Jakeman, and K. Ridley, "Phase statistics in non-Gaussian scattering," *J. Phys. A. Math. Gen.*, vol. 39, no. 24, pp. 7 621–7 640, Jun. 2006.

[7] R. Dusséaux and R. D. Oliveira, "Effect of the illumination length on the statistical distribution of the field scattered from one-dimensional random rough surfaces: Analytical formulae derived from the small perturbation method," *Waves Random Complex Media*, vol. 17, no. 3, pp. 305–320, Aug. 2007.

[8] K.-H. Ding, M. Rangaswamy, and L. Tsang, "Amplitude and phase distributions for bistatic scattering from Pierson-Moskowitz sea surfaces," in *Proc. IEEE Radar Conf.*, Rome, Italy, 2008, pp. 1–6.

[9] B. Gotwols and D. Thompson, "Ocean microwave backscatter distributions," *J. Geophys. Res.*, vol. 99, no. C5, pp. 9 741–9 750, May 1994.

[10] Y. Delignon, R. Garello, and A. Hillion, "Statistical modelling of ocean SAR images," *Proc. Inst. Elect. Eng.–Radar, Sonar Navigat.*, vol. 144, no. 6, pp. 348–354, Dec. 1997.

[11] A. Farina, F. Gini, M. Greco, and L. Verrazzani, "High resolution sea clutter data: Statistical analysis of recorded live data," *Proc. Inst. Elect. Eng.–Radar, Sonar Navigat.*, vol. 144, no. 3, pp. 121–130, Jun. 1997.

[12] I. Antipov, "Statistical Analysis of Northern Australian Coastline Sea Clutter Data," Defence Sci. Technol. Org. (DSTO), Edinburgh, Australia, Tech. Rep. DSTO-TR-1236, Nov. 2001.

[13] L. Rosenberg, D. Crisp, and N. Stacy, "Analysis of the KK-distribution with medium grazing angle sea-clutter," *Radar, Sonar Navigat.*, vol. 4, no. 2, pp. 209–222, Apr. 2010.

[14] K. Ward and S. Watts, "Use of sea clutter models in radar design and development," *Radar, Sonar Navigat.*, vol. 4, no. 2, pp. 146–157, Apr. 2010.

[15] J. Carretero-Moya, J. Gismero-Menoyo, A. B. del Campo, and A. Asensio-Lopez, "Statistical analysis of a high-resolution sea-clutter database," *IEEE Trans. Geosci. Remote Sens.*, vol. 48, no. 4, pp. 2 024–2 037, Apr. 2010.

[16] K. Ward, S. Watts, and R. Tough, *Sea Clutter: Scattering, the K-Distribution and Radar Performance*. Herts, U.K.: Inst. Eng. Technol., 2006.

[17] T. Elfouhaily, B. Chapron, K. Katsaros, and D. Vandemark, "A unified directional spectrum for long and short wind-driven waves," *J. Geophys. Res.*, vol. 102, no. C7, pp. 15 781–15 796, Jul. 1997.

[18] G. Trunk, "Radar properties of non-Rayleigh sea clutter," *IEEE Trans. Aerosp. Electron. Syst.*, vol. AES-8, no. 2, pp. 196–204, Mar. 1972.

[19] J. Toporkov and M. Sletten, "Statistical properties of low-grazing range-resolved sea surface backscatter generated through two-dimensional direct numerical simulations," *IEEE Trans. Geosci. Remote Sens.*, vol. 45, no. 5, pp. 1181–1197, May 2007.

[20] A. Coatanhay, "Statistical analysis of the electromagnetic field scattered by the ocean surface in various weather conditions: A numerical study in L-band," in *Proc. IEEE Int. Geosci. Remote Sens. Symp.*, 2008, vol. 1, pp. I-292–I-295.

[21] F. Nouguier, C.-A. Guérin, and B. Chapron, "Scattering from nonlinear gravity waves: The "choppy wave" model," *IEEE Trans. Geosci. Remote Sens.*, vol. 48, no. 12, pp. 4 184–4 192, Dec. 2010.

[22] C. Bourlier and G. Berginc, "Microwave analytical backscattering models from randomly anisotropic sea surface—Comparison with experimental data in C and Ku bands," in *Progress in Electromagnetics Research*, vol. 37, D. J. A. Kong, Ed. Cambridge, MA, USA: EMW Publishing, 2002, pp. 31–78.

[23] T. Elfouhaily and C.-A. Guérin, "A critical survey of approximate scattering wave theories from random rough surfaces," *Waves Random Media*, vol. 14, no. 4, pp. R1–R40, Oct. 2004.

[24] T. Elfouhaily, S. Guignard, R. Awadallah, and D. Thompson, "Local and non-local curvature approximation: A new asymptotic theory for wave scattering," *Waves Random Media*, vol. 13, no. 4, pp. 321–337, Oct. 2003.

[25] F. Nouguier, C.-A. Guérin, and G. Soriano, "Analytical techniques for the Doppler signature of sea surfaces in the microwave regime—I: Linear surfaces," *IEEE Trans. Geosci. Remote Sens.*, vol. 49, no. 12, pp. 4856–4864, Dec. 2011.

[26] H. Masuko, K. Okamoto, M. Shimada, and S. Niwa, "Measurement of microwave backscattering signatures of the ocean surface using X band and Ka band airborne scatterometers," *J. Geophys. Res.*, vol. 91, no. C11, pp. 13 065–13 083, Nov. 1986.

[27] M. W. Long, *Radar Reflectivity of Land and Sea*. Norwood, MA, USA: Artech House, 2001.

[28] J. Wright, "A new model for sea clutter," *IEEE Trans. Antennas Propag. [legacy, pre—1988]*, vol. AP-16, no. 2, pp. 217–223, Mar. 1968.

[29] G. Valenzuela, "Theories for the interaction of electromagnetic and oceanic waves—A review," *Boundary-Layer Meteorol.*, vol. 13, no. 1–4, pp. 61–85, Jan. 1978.

[30] G. Brown, "Backscattering from a Gaussian-distributed perfectly conducting rough surface," *IEEE Trans. Antennas Propag.*, vol. 26, no. 3, pp. 472–482, May 1978.

[31] F. Bass and I. Fuks, *Wave Scattering From Statistically Rough Surfaces*. Oxford, U.K.: Pergamon, 1978.

[32] N. Pinel, B. Chapron, C. Bourlier, N. de Beaucoudrey, and A. Ghaleb, "Study of RAR backscattered field statistics from sea surfaces under moderate winds," in *Proc. Ocean Coastal Observation, Sensors Syst.*, Brest, France, June 2010.

[33] N. L. Johnson, S. Kotz, and N. Balakrishnan, *Distribution in Statistics: Continuous Univariate Distributions, Volume I,* 2nd ed. Hoboken, NJ, USA: Wiley, 1994.

[34] Y. Delignon and W. Pieczynski, "Modeling non-Rayleigh speckle distribution in SAR images," *IEEE Trans. Geosci. Remote Sens.*, vol. 40, no. 6, pp. 1430–1435, Jun. 2002.

Nicolas Pinel (M'12) was born in Saint-Brieuc, France, in 1980. He received the Engineering degree and the M.S. degree in electronics and electrical engineering from Ecole polytechnique de l'université de Nantes (Polytech Nantes), Nantes, France, in 2003 and the Ph.D. degree from the University of Nantes, Nantes, in 2006.

He was a Research Engineer with the IETR Laboratory, Institut d'Électronique et de Télécommunications de Rennes, Nantes, at the time of the paper submission and recently joined Alyotech TS&I, Rennes, France. His research interests are in the areas of radar and optical remote sensing, scattering, and propagation. In particular, he works on asymptotic methods of electromagnetic wave scattering from random rough surfaces and layers.

Bertrand Chapron received the B.Eng. degree from the Institut National Polytechnique de Grenoble, Grenoble, France, in 1984 and the Ph.D. degree in physics (fluid mechanics) from the University of Aix-Marseille II, Marseille, France, in 1988.

He spent three years as a Postdoctoral Research Associate with the NASA Goddard Space Flight Center, Greenbelt, MD, USA, and the Wallops Flight Facility, Wallops Island, VA, USA. He is a Research Scientist and is currently the Head of the Spatial Oceanography Group, Laboratoire d'Océanographie Spatiale, Institut Français de Recherche et d'Exploitation de la Mer, Plouzané, France, where he is responsible for the Centre ERS Archivage et Traitement. He was a Coinvestigator and Principal Investigator in several European Space Agency (e.g., Envisat and Global Navigation Satellite System), NASA, and CNES (Topex/Poseidon and Jason) projects. He was also coresponsible (with H. Johnsen of NORUT) for the Envisat ASAR-wave mode algorithms and scientific preparation for the Envisat wind and wave products. He has experience in applied mathematics, physical oceanography, and electromagnetic wave theory and its application to ocean remote sensing.

Christophe Bourlier (A'08) was born in La Flèche, France, on July 6, 1971. He received the M.S. degree in electronics from the University of Rennes, Rennes, France, in 1995 and the Ph.D. degree from the Système Électronique et Informatique (SEI) Laboratory, Nantes, France, in 1999.

While at the University of Rennes, he was with the Laboratory of Radiocommunication, where he worked on antenna coupling in the VHF-HF band. He is currently with IREENA Laboratory (Institut de Recherche en Électrotechnique et Électronique de Nantes Atlantique), Polytech Nantes (University of Nantes), Nantes, France. He is an Assistant Researcher with the National Center for Scientific Research, working on electromagnetic wave scattering from rough surfaces and objects for remote sensing applications. He is the author of more than 90 journal articles and conference papers.

Nicole de Beaucoudrey was born in 1954. She received the Ph.D. degree in physics from the University of Paris XI, Orsay, France, in 1979.

She has been a Researcher with the Centre National de la Recherche Scientifique (CNRS) since 1979. She was with the Institut d'Optique, Orsay, until 1999. She is now with IREENA (Institut de Recherche en Électrotechnique et Électronique de Nantes Atlantique), University of Nantes, Nantes, France. Her present research interests include electromagnetic scattering and the resonance region.

René Garello (M'85–SM'96–F'06) was born in 1953. He received the Ph.D. degree in signal processing from the Institut National Polytechnique de Grenoble (INPG), Grenoble, France, in 1981 and the Habilitation (HDR; Habilitation to Supervise Research) in 1995.

From 1982 to 1984, he was a Research Associate with the Aeronomy Laboratory, National Oceanic and Atmospheric Administration, Boulder, CO, USA. He joined the Ecole Nationale Supérieure des Télécommunications de Bretagne (Telecom Bretagne), Brest, France, in 1985, where he has been a Professor in the field of signal processing and image processing since 1988. At Telecom Bretagne, he is the head of the research team TOMS (Traitement, Observations et Méthodes Statistiques—Processing, Observations, and Statistical Methods) within the CNRS unit LabSTICC before creating the ICTO (ICT for Ocean) program. For the last two decades, he has worked in the development of signal and image processing tools for the interpretation of radar signals and the extraction of sea surface features, either natural (wind, waves, and currents) or manmade (ships and pollution). These application fields were supported by several European projects and industrial contracts. He had supervised more than 30 Ph.D. students. He is the author of more than 40 papers, 130 conference communications, and 3 books. His main research interests lie in remote sensing, 2-D signal processing, and statistical and spectral analysis applied to ocean-surface-feature detection and characterization.

For all his works, Prof. Garello was elevated to the grade of Fellow of the IEEE, class of 2006, "for contributions to signal processing applied to remote sensing of the ocean." He was an elected IEEE Oceanic Engineering Society AdCom member from 1999 to 2001, from 2003 to 2005, and in 2005 for a new three-year term. In 2005, he was elected Vice-President Conference Operations and then reelected in 2006 and 2008. In the beginning of 2001, he headed the committee for defining a new set of conference policies and procedures in order to ensure continuity between successive OCEANS conferences. This committee (so-called JOAB—Joint OCEANS Administrative Board) defined several new approaches and came up with the concept of two-Oceans-a-year (every year in Northern America, every other odd year in Europe, and every other even year in Asia-Pacific). In 2012, he was elected President of the IEEE OES for a two-year term. He was the General Chairman of the First OCEANS of the new Two-Oceans-a-year concept: OCEANS'05 held in Brest, France, in June 2005. He received the OES Service Awards in 2006 for developing and implementing the two-OCEANS conference policy.

Antoine Ghaleb was born in France in 1980. He received the M.Eng. degree in computer science from ESME Paris, Paris, France, in 2003, the M.Sc. degree in remote sensing from the University of Paris Diderot, Paris, in 2004, and the Ph.D. degree in signal processing from Télécom ParisTech, Paris, until 2009.

While working on his Ph.D. dissertation, his research has focused on micro-Doppler analysis of nonstationary moving targets. The analysis of human motion in high-resolution radar imaging, both in range and Doppler, was his main center of interest. Since 2009, he has been a Research Engineer with the Radar Division, ARTAL, Brest, France, managing the MODENA project, a program aimed at modeling and simulating the maritime environment remotely sensed by radar. He is involved in R&D projects related to radar signal and image processing.